Langmuir

Article

pubs.acs.org/Langmuir

Interaction of Rh with Rh Nanoparticles Encapsulated by Ordered Ultrathin TiO_{1+x} Film on TiO_2(110) Surface

A. Berkó,*[,†] R. Gubó,[‡] L. Óvári,[†] L. Bugyi,[†] I. Szenti,[‡] and Z. Kónya[†,‡]

[†]MTA-SZTE Reaction Kinetics and Surface Chemistry Research Group, The Hungarian Academy of Sciences, University of Szeged, P.O. Box 168, H-6701 Szeged, Hungary

[‡]Department of Applied and Enviromental Chemistry, University of Szeged, Rerrich Béla tér 1, H-6720 Szeged, Hungary

ABSTRACT: Rh films of 5−50 monolayers (ML) were grown on TiO_2(110)−(1 × 1) surface by physical vapor deposition (PVD) at 300 K followed by annealing at max. 1050 K. In the coverage range of 5−15 ML, separated stripe-like Rh nanoparticles of approximately 30 × 150 nm lateral size and 10−20 layer thickness with a flat top (111) facet were formed. At higher coverages (15−50 ML), the Rh film sustained its continuity at least up to 950 K. For both cases, the Rh(111) top facets were completely covered by a long-range ordered hexagonal "wagon-wheel" TiO_{1+x} ultrathin oxide (hw-TiO-UTO) film. STM-STS, XPS, LEIS, and TDS methods were used for morphologic and electronic characterization of surfaces prepared in this way. The main part of this study is devoted to the study of postdeposition of Rh on the hw-TiO-UTO layer at different temperatures (230 K, 310 K, 500 K) and to the effect of subsequent annealing. It was found that 2D nanoparticles of 0.2−0.3 nm height and 1−2 nm diameter are formed at RT and their average lateral size increases gradually in the range of 300−900 K. The LEIS intensity data and the CO TDS titration of the particles have shown that an exchange of the postdeposited Rh atoms with the hw-TiO-UTO layer proceeds to an extent of around 50% at 230 K and this value increases up to 80−90% in the range of 300−500 K. The total disappearance of the characteristic LEIS signal for Rh takes place at around 900 K where a complete hw-TiO-UTO adlayer forms on top of the postdeposited metal (100% exchange).

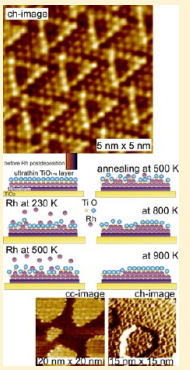

1. INTRODUCTION

The recent interest in macroscopic size, self-supporting 2D nanomaterials of atomic thickness like graphene[1,2] and newly found MoS_2 monolayer sheets[3] generated huge research activity also in related fields like self-organized fabrication of ultrathin 2D polymers,[4] formation of atomically thin oxide layers for advanced metal-oxid-metal (MOM) structures[5,6] and the ultrathin oxide (UTO) films formed by encapsulation of oxide-supported metal nanoparticles by thermal activation.[7−13] Regarding the two latter cases, clarification of the structural and electronic properties of UTO layers grown on metal substrates is of huge relevance in different fields of nanotechnology like nanoelectronics, gas-sensorics, or nanocatalysis.[11,14−16] The history of the discovery of self-organized and self-limited UTO films goes back to a very exciting phenomenon in heterogeneous catalysis, namely, to the formation of encapsulation layers on late transition metal nanoparticles supported on reducible oxide surfaces, termed SMSI (strong metal support interaction).[17−19] This phenomenon was also studied on inverse catalysts as model systems, where atomically thin metal oxide layers were formed on a metal single crystal surface.[16,20,21] The relation between the self-limiting encapsulation film formed on supported noble metal nanoparticles and the formation of ultrathin layers produced by oxidative deposition was studied in detail for the Pt/TiO_2 system.[22−27] It was recognized that ordered UTO film phases formed on supported metal nanoparticles by encapsulation (decoration) processes can also be produced on macroscopic metal surfaces via oxidative deposition under appropriate experimental conditions (oxygen pressure, temperature, etc.).[23,25,28]

The formation of strongly reduced oxide films of "wagon-wheel" or "zig-zag" like symmetry is quite typical for several oxide-metal systems both in the case of TiO_2-supported Pd,[7,30,31] Pt,[8] and Rh[10,29] nanocrystallites and in the case of oxide films prepared on metal single crystals like TiO_{1+x}/Pt(111),[23,25,26,32] TiO_{1+x}/W(110),[28] TiO_{1+x}/Rh(111),[33] VO_{1+x}/Pd(111),[34] and VO_{1+x}/Rh(111).[21,35] The chemical contrast detected for the "wagon-wheel" ultrathin metal oxide films of hexagonal structure (hw-MO-UTO) were also the subject of several theoretical works.[16,23,24,32,35] A further interesting aspect of the UTO films is the formation of ordered metal adlayers on epitaxial oxide films by lattice controlled nucleation and growth.[14,16,24,36−38] The mass transport processes of an admetal depend strongly on the actual structure of the UTO layer, which has nowadays received special attention.[14,24,39−42]

The study of growing Pt nanoparticles on a TiO_2(110) support at high temperatures suggested that the ultrathin decoration TiO_{1+x} film is continuously renewed during the process.[43] The present work is devoted to understanding the elementary steps of this process at atomic scale for the Rh/TiO_2(110) system by measuring the temperature and coverage effects of Rh postdeposition. In a recent paper, we have already

Received: October 15, 2013
Revised: November 25, 2013

   dx.doi.org/10.1021/la4038292 | *Langmuir* XXXX, XXX, XXX−XXX

studied the formation of Rh overlayers on ultrathin encapsulation titania films by spectroscopic methods like Auger-electron spectroscopy (AES), low energy ion scattering (LEIS), X-ray photoelectron (XPS), and thermal desorption spectroscopy (TDS), and moreover, work funtion (WF) measurements.[44] In order to understand better the atomic scale processes of this system, we report here on the investigation of postdeposition of Rh on the ordered TiO_{1+x} "wagon-wheel" structure produced on large Rh crystallites supported on the TiO_2(110) surface. The experimental facilities used here were scanning tunneling microscopy/spectroscopy (STM/STS) and LEIS, XPS, and TDS techniques.

2. EXPERIMENTAL SECTION

The STM measurements were carried out in a UHV system evacuated down to 5×10^{-8} Pa equipped with a scanning tunneling microscope (WA-Technology) and a cylindrical mirror analyzer (Staib-DESA-100). The LEIS, XPS, and TDS measurements were performed in another chamber furnished with a hemispherical electron energy analyzer (Leybold Heraus) and a quadrupole mass spectrometer (Balzers-Prisma). Commercial Ar^+ guns were applied for cleaning and e-beam evaporators for metal deposition. Using Pt–Ir tips, the STM images were generally recorded in constant current (cc) mode at a bias of +1.5 V on the sample and a tunneling current of 0.1 nA. The conditioning of the tip was performed by tunneling at U_{bias} = +10 V and I_t = 1.0 nA for several seconds. Images of enhanced lateral resolution were taken up in constant height (ch) mode. For some images, a moderate FFT treatment was also applied. The *X-Y-Z* calibration of the STM images was performed by measuring the characteristic morphological parameters of the TiO_2(110)-(1 × 1) support (lateral unit cell 0.296 nm × 0.650 nm, height of the steps 0.297 nm). The error of the morphological data obtained and presented in this work is below ±3%. A SPECS IQE 12/38 ion source was used for LEIS. He^+ ions of 800 eV kinetic energy were applied at a low ion flux equal to 0.03 $\mu A/cm^2$. The incident and detection angles were 50° (with respect to the surface normal), while the scattering angle was 95°. The angle between the "incident plane" (the plane defined by the ion source axis and the surface normal) and the "detection plane" (the plane defined by the surface normal and the analyzer axis) was 53°. LEIS and XPS spectra were obtained using the same Leybold hemispherical analyzer and applying an Al–Kα X-ray source in the latter case. The binding energy scale was calibrated by the $4f_{7/2}$ peak of a thick Au layer, fixed at 84.0 eV. If not mentioned otherwise, the takeoff angle (θ) was 16° with respect to surface normal. During TDS measurements, the sample was in line of sight position and the heating rate was below 2 K s^{-1}.

In the STM chamber, an epi-polished rutile TiO_2(110) single crystal of 5 × 5 × 1 mm^3 were directly fixed to a Ta filament by an oxide adhesive (Aremco 571) and it was mounted on a transferable sample holder cartridge. The probe was indirectly heated by the current flowing through the Ta filament. The temperature of the probe was measured by a chromel-alumel (K-type) thermocouple stuck to the side of the sample by the same oxide adhesive. In the XPS-LEIS-TDS chamber, a similar probe with a slightly different mounting was applied in order to cool the probe down to ~230 K. For both cases, the sample cleaning was started by a gradual increase of the temperature up to 1050 K followed by Ar^+ bombardment (1.5 keV, 4–6 $\mu A\ cm^{-2}$) and annealing cycles at 1050 K. For the measurements presented in this work, bulk terminated (1 × 1) surface decorated by 0D dot and 1D stripes (reduced Ti_2O_3 phase) of low concentration were applied.[45] The deposition rate of Rh was typically 0.5 ML/min. Special attention was paid to the cross-calibration of the Rh coverages in the two chambers by Auger-electron spectroscopy uptake curves recorded at 300 K. In the XPS-LEIS-TDS chamber, the metal coverages were checked also by XPS and a quartz crystal microbalance. The estimated coverage values agreed within a precision of 10%.

3. RESULTS

3.1. Formation of Stripe-Like Encapsulated Rh Nanoparticles on TiO_2(110) Surface. Figure 1 shows STM cc-

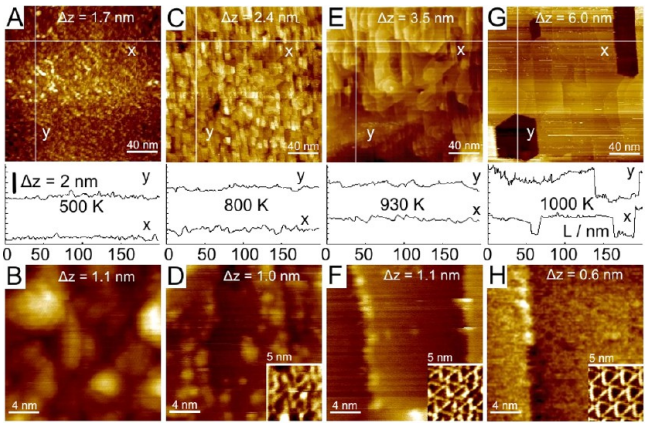

Figure 1. Effects of thermal treatment on the morphology of TiO_2(110) surface deposited by ~30 ML of Rh at 320 K and annealed at (A, B) 500 K, (C, D) 800 K, (E, F) 930 K, and (G, H) 1000 K for 10 min. The size of STM cc-images: (A, C, E, G) 200 × 200 nm^2, (B, D, F, H) 20 × 20 nm^2. The inserted ch-images of 5 × 5 nm^2 (D, F, H) exhibit the atomic scale details of the extended terraces. The height (z) profiles plotted under the corresponding images were detected along the lines indicated in the STM images (A, C, E, G).

images of 200 × 200 nm^2 (A, C, E, G) and 20 × 20 nm^2 (B, D, F, H) recorded after the deposition of approx 30 ML Rh at room temperature (RT) and annealed at (A, B) 500 K, (C, D) 800 K, (E, F) 930 K, and (G, H) 1000 K for 10 min, respectively. The inserted ch-images of 5 × 5 nm^2 in D, F, H show the terrace structure at high resolution. The line profiles measured along x and y directions indicated on the corresponding STM images (A, C, E, G) are also plotted in Figure 1. The surface shows a corrugation of only few atomic layers (<1 nm) at 500 K (Figure 1A) indicating that all the deeper layers are more or less complete and buried. The average size of the atomic terraces is rather small, less than 3 nm, and the step site (atom) density is very high, in the range of approx 10^{13}–10^{14} cm^{-2} (Figure 1B). Annealing at 800 and 930 K causes a gradual increase of the average terrace size up to 5 and 15 nm, respectively (Figure 1C–F). Accordingly, the step site density decreases significantly down to 10^{12} cm^{-2}. A dramatic change of the surface morphology appears only after 10 min annealing at 1000 K where rather large atomic terraces of 30 nm are formed and very deep hexagonal and [001] elongated pits of 50–70 nm in length appear simultaneously (Figure 1G). The bottom of these pits indicates the height level of the supporting oxide surface. A similar behavior, an opening of a continuous Pd multilayer, was also reported for Pd/TiO_2(110) system.[7] The diffusion mechanism (Brandon-Bradshaw's model) governing this process was recently analyzed in detail.[46] Annealing at higher temperatures results in splitting of the continuous Rh multilayer into stripe-like Rh islands and leads to a TiO_2(110) surface covered partially by Rh islands exhibiting flat top facet (see below). This morphology provide a chance to follow the (post)deposition of Rh both on the top facet of Rh nanoparticles and on bare TiO_2(110) terraces in parallel. The inserted STM ch-images of 5 × 5 nm^2 (Figure 1 D, F, H) show that the top facets exhibit a totally different nanostructure from that detectable on a clean Rh(111)

dx.doi.org/10.1021/la4038292 | *Langmuir* XXXX, XXX, XXX–XXX

surface and it can be identified with the ordered encapsulation TiO_{1+x} layer (hexagonal "wheel" TiO_{1+x} ultrathin oxide film, hw-TiO-UTO).[10] The lateral ordering of this film develops gradually with the annealing temperature. It is already almost complete at 800 K, although this arrangement becomes nearly perfect only after the annealing above 900 K.

STM images of 400 × 400 nm^2 are shown in Figure 2A,B, where the clean TiO_2(110) surface was exposed to two

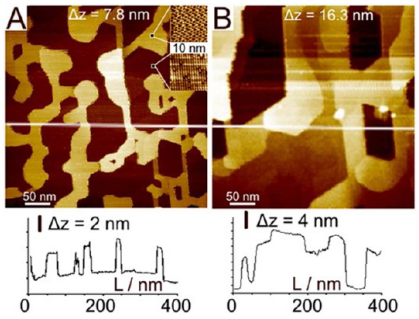

Figure 2. Characteristic surface morphology detectable on TiO_2(110) by STM after deposition of two different amount of Rh (A) 7 ML and (B) 30 ML at 320 K followed by annealing at 1050 K for 10 min. The inserted ch-images of 10 × 10 nm^2 in A exhibit the atomic scale structures appearing on top facets of surface Rh and on clean TiO_2(110) terraces. The *z*-profiles plotted under the corresponding images of 400 × 400 nm^2 exhibit the variation of height levels along the lines indicated in the images.

different amounts of Rh (approx 7 ML and 30 ML) at room temperature and annealed at 1050 K for 10 min. The line profiles recorded along the stretches indicated in the images are drawn at the bottom of the figures where the *x*−*y* scales are the same in each case. The inserted ch-images of 10 × 10 nm^2 in Figure 2A depict the surface of Rh top facet (bright regions) and that of the free TiO_2(110) terraces (dark regions). In the experiments presented below, similar surfaces like that presented in Figure 2A were used as an initial configuration for the Rh postdeposition experiments. As can be seen, the bright Rh stripes are typically 20−30 nm wide and 5 nm high; accordingly, it is easy to find extended regions of at least 15 × 15 nm^2 size both on Rh top facets and on bare TiO_2(110) terraces (Figure 2A and the relating line profile). It is also appreciable that the elongation direction of the Rh particles is the same as the direction of parallel rows running in [001] crystallographic orientation of the support oxide and separated by 0.65 nm on the TiO_2(110)-(1 × 1) terraces.[10]

3.2. Characterization of the TiO_{1+x} Hexagonal Ultrathin Film Formed on Rh Nanoparticles Supported on TiO_2(110). In this section, the characteristics of the encapsulation layer formed on the top facets of the Rh stripes is described. The STM image (10 × 10 nm^2) in Figure 3A recorded in constant current mode (cc-image) shows that the top facets are rather flat and only a slight variation of the height in the range of the noise of our measurements (0.03 nm) can be detected. Much better contrast and lateral resolution can be achieved in constant height imaging mode (Figure 3B,C,D). In the course of our investigations, these three characteristic contrasts were observed for the TiO-UTO encapsulation layers. This variation in the contrast can be unambiguously explained by the different chemical state of the tip and not by the bias-current conditions or by the structural changes of the encapsulation layer. According to our experience, this series

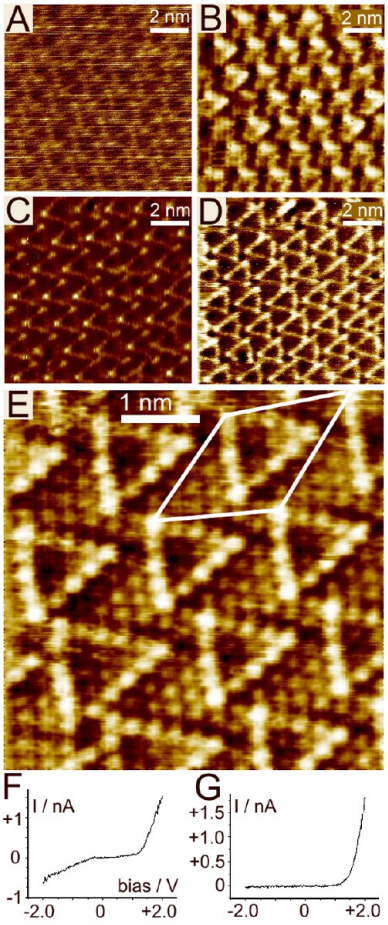

Figure 3. Atomic scale STM images of well ordered hw-TiO-UTO encapsulation layer recorded on the top facet of Rh particles for different imaging conditions: (A) cc-image (10 × 10 nm^2) of very small corrugation (<0.1 nm); (B,C,D) ch-images (10 × 10 nm^2) of several characteristic chemical contrast appeared during the course of this work. (E) ch-image of 5 × 5 nm^2 with an utmost lateral resolution and contrast achieved in this work. Characteristic STS spectra recorded on (F) hw-TIO-UTIOF layer and (G) TiO_2(110)-(1 × 1) stoichiometric terrace.

of images represents the gradual steps toward the atomic resolution presented in Figure 3E. This ch-image clearly exhibits a hexagonal overlayer lattice with an average lattice parameter of 0.31 (±3%) nm, although the points of the lattice are distorted by 10−20% from the ideal hexagonal positions. Note that the contrast of the points reveals a "wheel" structure similar to that described in our recent paper.[10] The average unit cell containing the complete wheel structure (superlattice) is nearly the same as detected previously (hexagonal, 1.5 nm × 1.5 nm). Nevertheless, the fine analysis of the dot intensities shows some obvious differences: (i) the side of the triangles of brighter contrast consists characteristically of 5 atoms (4 atomic distances) instead of 6 atoms, although regions also with this longer length coexist with the former arrangement (see Figure 3E, left bottom); (ii) the strict determination of the atomic positions of the oxide layer provided clear evidence for the lateral surface tension inducing displacements of the constituent Ti ions (bright points). The variation of the morphologic appearance of the "wheel" structure can probably be assigned to an ordered variation of the oxygen content in the TiO-UTO layer (see discussion below).[23] It is evident from our

dx.doi.org/10.1021/la4038292 | *Langmuir* XXXX, XXX, XXX−XXX

local tunneling spectrum taken above the encapsulation layer that the hw-TiO-UTO layer is a strongly reduced TiO_{1+x} form with a significantly lower forbidden gap (approx 1 eV) than that of the bulk terminated TiO(110)-(1 × 1) surface (3 eV) (Figure 3F,G). The filled states region (negative sample bias) exhibits a much higher tunneling current in the case of the TiO-UTO film, indicating a partial reduction of Ti ions compared to Ti^{4+} states on the stoichiometric TiO_2(110) terraces. We note that several times during our study we detected spontaneously formed pits of 2−3 nm average diameter and of 0.08 nm average depth in the encapsulation film. This observation suggested that it may be possible to remove or locally destroy the TiO-UTO film without causing serious damage of the underlying Rh atomic layers. The detailed results of this latter project will be published elsewhere; nevertheless, in Figure 4

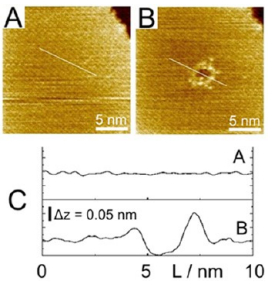

Figure 4. Effect of local excitation of the hw-TiO-UTO layer by tunneling tip: (A) constant current STM image of 20 × 20 nm^2 before the local treatment; (B) the same region detected by cc-imaging after generation of a crater-like nanostructure (for more details see the text). (C) Line profiles picked up in the regions indicated in A and B images.

we show an experiment relevant for the present work. The cc-image in Figure 4A shows a flat top facet region of 10 × 10 nm^2 of a Rh nanocrystallite encapsulated by hw-TiO-UTO. For the purpose of lateral identification, a monatomic step region can also be seen in the upper right part of the image (Figure 4A). The following parameters were used for a cc-imaging: +1.5 V (bias); 0.1 nA (tunneling current). After recording the STM image, the tip was moved to the center of the region. By holding the tunneling current at 0.1 nA, the bias was increased up to +4.8 V for 5 s. The imaging repeated with the same parameters as before shows a crater-like feature in the center of the image (Figure 4B). The line profile exhibits that the *z*-level of the inner region of the crater is lower by approx 0.06 nm than the flat region outside the crater (Figure 4C). Although this value is somewhat smaller than that measured for a spontaneously leaky film (0.08 nm), in first approximation the thickness of the hw-TiO-UTO layer can be estimated as 0.07 (±0.01) nm. Naturally, this value may strongly be influenced by electronic effects, which are not negligible in this height regime.

In parallel experiments, we also detected the characteristic LEIS and XPS spectra of the encapsulation layer (Figure 5). Regarding the STM results presented above in Figure 1, the Rh layer of approx 30 ML thick (or thicker) formed on TiO_2(110) at RT retains its continuity during thermal treatments at least up to 930 K. This fact enables the successful application of area-averaging techniques, like LEIS, AES, and XPS, for a clear chemical characterization of the encapsulation hw-TiO-UTO film.[44] In Figure 5A, LEIS spectra (i) show that the topmost atomic layer consisted only of Rh after the evaporation of 37 ML rhodium at RT. Subsequent annealing at 930 K, however, results in a complete disappearance of the Rh peak and the

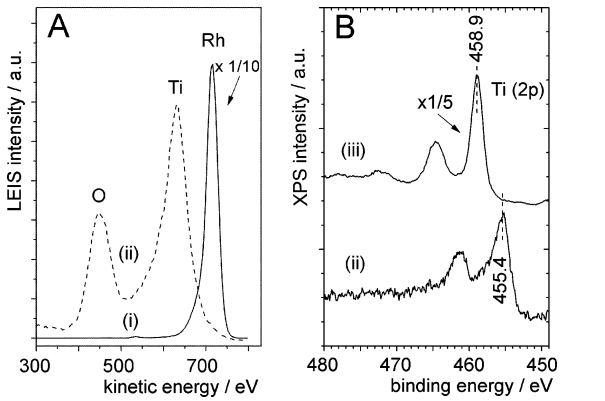

Figure 5. (A) LEIS spectra of the TiO_2(110) surface taken (i) after the deposition of 37 ML of Rh at 300 K and (ii) followed by annealing at 930 K for 5 min; (B) the Ti 2p XPS region recorded (ii) after the deposition of 37 ML Rh onto a clean TiO_2(110) surface followed by 5 min annealing at 930 K and (iii) on a clean TiO_2(110) surface.

spectrum (ii) is exclusively dominated by the Ti and O peaks, indicating clearly the formation of a TiO_{1+x} encapsulation layer. This result is in good harmony with the STM measurements presented above. The position of the Ti $2p_{3/2}$ peak (455.4 eV) of the encapsulation layer shown by XPS curve (ii) in Figure 5B and its relative position (ΔE = 3.5 eV) with respect to that measured in the case of the nearly stoichiometric TiO_2(110) surface (458.9 eV) presented by curve (iii) clearly suggests an oxidation state of Ti^{2+} for the distinct majority of Ti sites.[47,48] The dominance of the Ti 2p region by the Ti^{2+} component suggests that the stoichiometry was not far from O:Ti = 1. Comparing the O(1s)/Ti(2p) area ratio of the TiO_2(110) surface with the corresponding ratio of the encapsulating layer suggests a stoichiometry of O:Ti = 1.2 (±0.1). The lack of a visible Ti^{4+} component in spectrum Figure 5B (ii) is in accordance with former observation of TiO_{1+x} encapsulation layer on Rh crystallites and with the STM measurements (Figure 1E) indicating that dewetting of the Rh film formed on TiO_2(110) does not set in at 930 K.

3.3. Deposition of Rh onto a TiO_2(110) Surface Partially Covered by Stripe-Like Rh Particles Encapsulated by hw-TiO-UTO; the Effects of Thermal Treatment.

Figure 6 displays some characteristic constant current and constant height STM images of (A, C, E, G, H, I) 10 × 10 nm^2 and (B, D, F) 5 × 5 nm^2, respectively, recorded before (A−B) and after (C−D) Rh postdeposition of very low coverage (∼0.03 ML) at RT followed by annealing at different temperatures for 10 min: (E−F) 600 K, (G) 900 K, (H) 950 K, (I) 1050 K. Note that this coverage represents a surface adatom concentration belonging approximately to the characteristic surface density of the wagon-wheel unit cells (4 × 10^{13} cm^{-2}). This is the concentration where the so-called templating behavior, if there is such an effect attributable to the so-called picoholes, could be clearly revealed by STM.[24] Figure 6A (cc-image) shows the top facet of the encapsulated Rh nanoparticles before the postdeposition of Rh. The very low overall corrugation (0.3 nm) of this image suggests a very flat surface with a low concentration of dot-like defects like in the center bottom of the image. The flat region of a top facet exhibits a typical "wheel" pattern of significant chemical contrast recorded by ch-imaging (Figure 6B). The Rh deposition results in the appearance of new protrusions with a diameter of less than 1 nm and height of ∼0.2 nm (Figure 6C). These structures can

dx.doi.org/10.1021/la4038292 | Langmuir XXXX, XXX, XXX−XXX

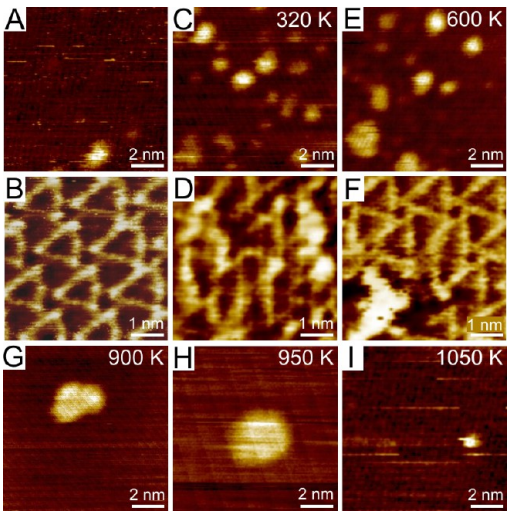

Figure 6. Effects of the deposition of Rh at zero coverage limit (~0.03 ML) onto hw-TiO-UTO encapsulation layer and that of stepwise annealing for 10 min. STM images recorded in cc and ch mode (A,B) before Rh postdeposition, (C,D) after deposition of ~0.03 ML of Rh at 320 K, and (E,F) after the subsequent annealing at 600 K. The size of cc-images A, C, E is 10 × 10 nm^2 and that of ch-images B, D, F is 5 × 5 nm^2. The effects of further annealing at (G) 900 K, (H) 950 K, and (I) 1050 K. The size of the latter cc-images is 10 × 10 nm^2.

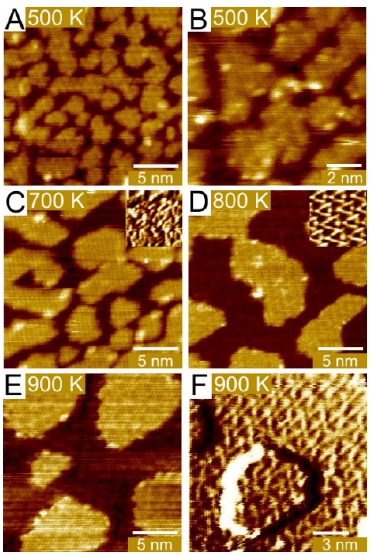

Figure 7. Effects of Rh deposition onto hw-TiO-UTO surface in the monolayer regime (~1.5 ML) and that of stepwise annealing for 10 min. STM cc-images were recorded (A,B) after Rh postdeposition at 500 K and following thermal treatments at (C) 700 K, (D) 800 K, and (E) 900 K. The size of cc-images: (A,C,D,E) 20 × 20 nm^2, (B) 10 × 10 nm^2. Inserted ch-images in C (10 × 10 nm^2) and D (5 × 5 nm^2) were taken on the top of 2D clusters after the thermal treatments at 700 and 800 K, respectively. The ch-image (F) of 15 × 15 nm^2 was recorded on the sample annealed at 900 K.

be indentified with 2D clusters consisting of 8−10 atoms. In the corresponding ch-image (Figure 6D), it can be seen that the "wheel" net is strongly perturbed although some ordering is still visible. The subsequent annealing at 600 K for 10 min results in a moderate increase of the average diameter of the 2D protrusions accompanied by a slight decrease of their surface concentration (Figure 6E), and the wheel pattern becomes again more or less perfect (Figure 6F). Upon annealing at higher temperatures (900 K, 950 K), the sintering of the 2D adparticles continues probably due to a 2D Ostwaldt ripening process. This growth kinetics results in 2D nanoparticles of ~3 nm, while their outline becomes round-shaped (Figure 6G,H). The LEIS measurements have shown that these particles contain only Ti and O ions (see below). Annealing at the highest temperature applied in this work (1050 K) leads to the complete disappearance of the adparticles from the surface (Figure 6I). This latter observation can be explained by dissolution of the largest adparticles into the bulk of the Rh stripes.

In the subsequent experiments, the main features revealed above are confirmed by deposition of a higher amount of Rh (approx 1.5 ML) at 500 K followed by annealing at higher temperatures (Figure 7). It needs to be noted that the estimation of Rh coverage was performed by measuring the total volume of extra particles appeared both on Rh top facets and on Rh-free terraces of TiO_2(110). The deposition of approx 1.5 ML of Rh at 500 K resulted in dendrite-like 2D nanoparticles with a characteristic height of 0.2−0.3 nm (Figure 7A). Although the particles are seemingly flat on 20 × 20 nm^2 cc-images, their top facet exhibits a complex composition on the magnified images of 10 × 10 nm^2 (Figure 7B). The thermal treatments at 700, 800, and 900 K resulted in a gradual sintering of the nanoparticles without changing their height (Figure 7A,C,D,E). The inserted ch-images of 10 × 10 nm^2 and 5 × 5 nm^2 depict the chemical contrast of the top facets after thermal treatments at 700 and 800 K, respectively (Figure 7C,D). It is clear that this is the temperature range where the unordered TiO-UTO layer transforms into an ordered "wheel" phase. For the annealing at 900 K, a ch-image of 15 × 15 nm^2 recorded in the region of an added particle shows clearly that both the empty and the adparticle-occupied regions exhibit well ordered "wheel" structure (Figure 7F).

The morphological characteristics of Rh/TiO_2(110) samples applied as an initial configuration in this work made it possible to follow the effect of the same Rh postdeposition and sample treatment both on the top facet of the Rh particles and on the Rh-free TiO_2(110) terrace regions. The STM cc-images of 20 × 20 nm^2 in Figure 8A,B show the surface morphology on the top facet of stripe-like Rh nanoparticle for two different Rh depositions: (A) ~0.03 ML, (B) ~1.50 ML at RT followed by annealing at 800 K for 10 min. For both coverages, the nanoparticles exhibit noncircular outlines with some preferred directions (threefold symmetry) well visible at the higher coverage (B). One of these preferred directions fits well to the [001] crystallographic orientation of the support TiO_2(110) as indicated on images B and C. Note that the elongated side of the stripe-like Rh particles also fits this orientation. The line profiles measured and indicated on the corresponding images can be seen in Figure 8E. The height of these particles is quite uniform, 0.2−0.3 nm. As was shown above, the top facet of these adparticles consists mainly of the hw-TiO-UTO layer, which covers the Rh nanoparticles formed by postdeposition of Rh (see Figure 7D,F). Naturally, in parallel to the formation of adparticles on the Rh stripes, nanoparticles are also formed on the Rh-free TiO_2(110) surface. The STM cc-images recorded in these latter regions are shown in Figure 8C,D. In the case of lower Rh coverage (~0.03 ML), the height of the adparticles is in the range of 0.3−0.5 nm, which means that these particles consist of at least 2−3 layers (Figure 8C,E). In the case of higher coverage (~1.5 ML), the 3D nanoparticles formed on

dx.doi.org/10.1021/la4038292 | Langmuir XXXX, XXX, XXX−XXX

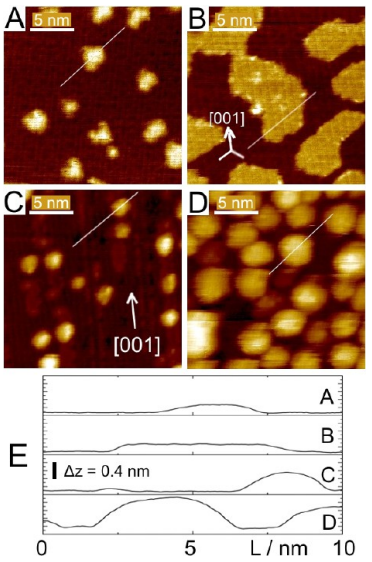

Figure 8. Comparison of nanoparticle formation followed simultaneously on (A,B) hw-TiO-UTO layer and (C,D) clean TiO_2(110) terraces. In both cases two different amounts of Rh (A,C) ~0.03 ML and (B,D) ~1.5 ML were deposited at 320 and 500 K, respectively, and followed by annealing at 800 K. The size of all these cc-images is 20 × 20 nm^2. (E) Collected line-profiles measured along the stretches indicated in the corresponding images.

the clean TiO_2(110) terraces consist of 4−5 layers (~1.0 nm) (Figure 8D,E).

3.4. Rh Postdeposition at Low Temperature (230 K) and the Effects of Annealing: LEIS and TDS Measurements. A spectroscopy study of the growth of Rh at room temperature (or at 500 K) on the top of an hw-TiO-UTO layer formed on a compact Rh thin film of 50 monolayers was already reported in a recent work.[44] Via detailed LEIS, AES, and work function (WF) measurements, it was shown that Rh exposed at 300 and 500 K leads to a linear increase in the Rh/Ti AES ratio and Rh LEIS signal intensity up to 1 ML coverage, suggesting the formation of Rh overlayer of unchanged thickness. This conclusion is strongly supported by the STM measurements presented in this work (section 3.3). The fact that the Rh LEIS signal disappears only at around 900 K also fits well to the complete ordering of the wh-TiO-UTO film detected by STM on the effect of annealing in the range of 800−900 K (Figure 7). The careful analysis of the LEIS intensity data has shown that following the Rh deposition at 300 and 500 K the majority of the Rh atoms bond to the upmost Rh layer (below the hw-TiO-UTO film) and is shadowed by unordered TiO_{1+x} layer. We estimate that only 10−15% of the adsorbed Rh atoms stay in the position detectable by LEIS. This feature can be explained by an exchange process during the deposition of Rh, requiring a relatively low activation energy. On the contrary, the encapsulation process which completes at around 900 K, accompanied by the formation of ordered hw-TiO-UTO layer as shown by STM, requires a significantly higher activation energy.[44] Since the energy available for thermal activation reduces by decreasing the deposition temperature, a suppression of the exchange/encapsulation process can be expected at deposition temperatures below 300 K. To check this effect, we addressed here the process of decoration at cryogenic temperatures. Lacking a low temperature STM facility in our laboratory, we present only LEIS and TDS data with a minimum deposition temperature of ~230 K.

Figure 9 displays the Rh LEIS intensity as a function of temperature for 0.8 ML Rh postdeposited at 230 K on an hw-

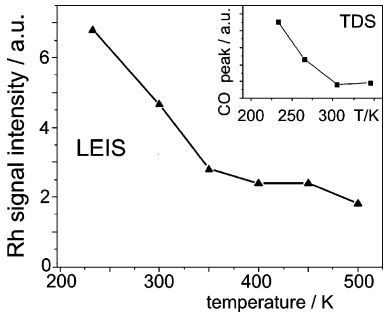

Figure 9. Change of Rh LEIS signal intensity upon annealing a hw-TiO-UTO covered Rh multilayer deposited by 0.8 ML Rh at 230 K. Inset: Change of CO uptake calculated from TDS peak areas as a function of the temperature, where the hw-TiO-UTO covered Rh multilayer deposited by 0.4 ML of Rh at 230 K was heated prior to saturation with CO (20 L) at 230 K.

TiO-UTO layer covering a 30 ML thick Rh film. The Rh signal decreases steeply up to 350 K, while further heating to 500 K results only in its slight decay. The analysis of the signal intensities indicates that the amount of Rh detectable by LEIS at 230 K is approximately 2−3 times larger than the amount of Rh present in the outmost layer after postdeposition at 500 K. In order to confirm this measurement by another technique, the adsorption and thermal desorption of CO was also investigated. First, the hw-TiO-UTO/Rh-multilayer system was postdeposited by 0.4 ML Rh at 230 K; subsequently, it was annealed up to a given temperature and then it was saturated with CO at 230 K. The amount of desorbed CO obtained by the integration of CO desorption peaks is plotted as a function of the annealing temperature (inset in Figure 9). A steep decrease of CO uptake was observed between 230 and 300 K, indicating the loss of adsorption capacity. Negligible change in the desorbed amount of CO was experienced on further annealing to 350 K. Obviously, the decrease in both Rh LEIS signals and CO adsorption capacity of Rh particles in the range of 230−350 K indicate that with an increase of the temperature, the postdeposited Rh particles become gradually encapsulated to a higher extent. Considering that it occurs below 350 K, it needs a significantly lower activation energy as compared to that for encapsulation on the nearly stoichoimetric titania, which starts at around 500−600 K, depending on the extent of reduction of the surfaces.[44,49]

4. DISCUSSION

4.1. Comparison of "Wagon-Wheel" Like UTO Layers Formed on Different Metals. The knowledge of the structural and chemical composition of ordered oxide ultrathin films accumulated in last years provides a chance to fit our specific results in the general picture of UTO/metal structures.[11,14−16,22,23,26,38,50] Independent of whether the UTO layer is supported on nanocrystallites or on macroscopic single crystal surfaces, an increasing number of works on UTO/metal systems have recently been published about a highly reduced "wagon-wheel" or "zig-zag" like ultrathin covering layer identified by STM and studied by theoretical calculations: hw-TiO-UTO on Pt(111),[23,26,37] Pd(111),[7,30,31] Rh(111),[10,29] and

dx.doi.org/10.1021/la4038292 | Langmuir XXXX, XXX, XXX−XXX

W(110)[28] surfaces, hw-VO-UTO on Pd(111)[34] and Rh(111),[21,35] hw-FeO-UTO on Pt(111),[50] hw-CrO-UTO on Pt(111).[51] Several comparative discussions of the "wagon-wheel" structures have also been published during the past years.[10,12,16,23,25,26,35,50] The common definition of these patterns was based on symmetry considerations, namely, a hexagonal overlayer structure with symmetry of *p6* grown and rotated by a θ angle on a *p6m* substrate.[26] The main feature of the "wagon-wheel" motifs are (i) the central dark dot (hub), (ii) the spoons forming bright triangles, and (iii) the brighter and darker dots providing a hexagonal overlayer lattice, as presented by Majzik et al.[10] and depicted here in Figure 10A. Note that the balls of different color in this sketch depict only the contrast relation of the structure shown in Figure 3. Although the pattern was fairly reproducible in our case, we observed two different contrasts (T6, T5) in some cases (see Figure 3E) as drawn in the left and right side in Figure 10A. On

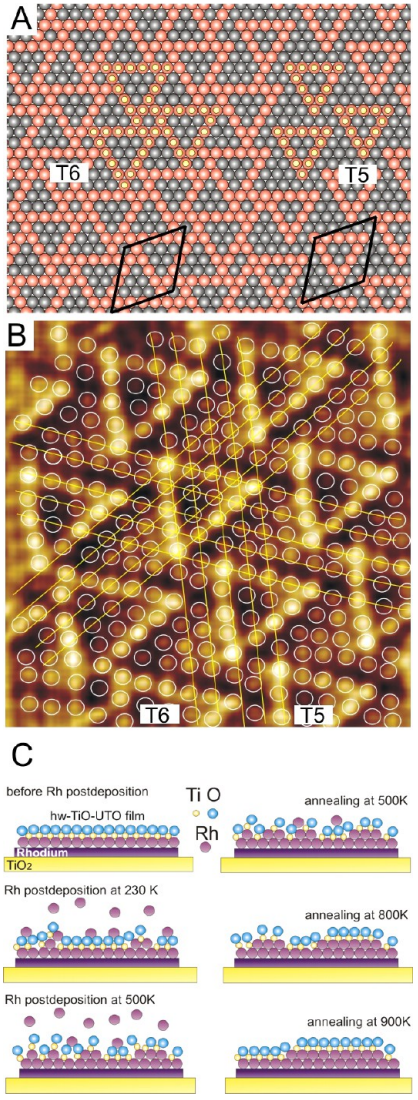

Figure 10. (A) Contrast scheme of hw-TiO-UTO layer found during the encapsulation Rh nanoparticles supported on TiO_2(110). (B) Distortion of the atomic positions found by STM in the hw-TiO-UTO layer (the lines are only to guide the eye). (C) Scheme for the rearrangement in the atomic layers for Rh deposited on hw-TiO-UTO layer and for the annealing at different temperatures.

the basis of some recent theoretical model calculations, the simple moire-pattern-based explanation of the contrast of the wagon-wheel pattern was replaced by a more complex model of this structure, in which a special lateral distribution of the surface oxygen atoms was considered.[11,16,23,25,26,37] Our results clearly support this latter idea, because we found that the periodicity of the overlayer lattice (0.31 nm) does not change for the two different patterns described above. Although the long-range periodicity (superlattice) observed for the different systems may be determined basically by the misfit between the surface and the overlayer lattice (moire-character), the balanced and inhomogeneous oxygen distribution allowing different oxidation states in the UTO layer plays also an important role. The overlayer lattice of hw-TiO-UTO on Rh(111) in our case can be interpreted as a complete mesh of Ti ions with an overall lattice constant of 0.31 (±0.01) nm (rotated by 2° relative to the Rh lattice) which does not show a defect site ("picohole") in the "hub" point of the "wheel" motif (Figure 3E).[23] It is especially true for the variant of this structure shown in the right side of Figure 10A, nevertheless, that the "picohole" feature cannot be excluded in the case of the other variant (Figure 10A, left side).[10] The STM image in Figure 10B (shown also in Figure 3E, as detected) has been treated by inverse Fourier-transformation for the better visibility and the atomic sites are marked by circles. The large chemical contrast among the sites appearing in the atomically resolved ch-images in this work can be attributed to the different oxygen coordination (fourfold and threefold) of the Ti ions arranged in the spoke rows (bright triangles) and in the other points of the "wheel" structure (Figure 10B), respectively, as recently interpreted by Barcaro and his coworkers.[23] Two important remarks should be made in connection with the image in Figure 10B: (i) "wagon-wheel" structures with different lengths of the bright spokes and with the same periodicity are simultaneously present and their registry fits with each other; (ii) although the appearance of the atomic sites detectable in the overlayer are almost complete, their exact registry is imperfect. This latter fact indicates a rather strong tension in the overlayer which is understandable because of the misfit to the support metal (Rh). There are regions where the distance between the individual adjacent atomic sites could deviate by 20−30% from the average lattice constant of 3.1 nm. Regarding the adsorption and reactivity of postdeposited Rh atoms, this latter fact is very important (see below). A similar overlayer lattice distortion was observed for hw-TiO-UTO/Pd(111) system, where the bending of the spokes was explained by a slight displacement of Ti ions toward the more stable threefold hollow positions of the Pd lattice.[30]

Regarding the chemical composition of the hw-TiO-UTO layer on Rh, the XPS, STS, and LEIS measurements presented in this work support clearly a Ti:O stoichiometry of close to 1, which is a widely accepted value for the "wagon-wheel" type ultrathin oxide films. The presence of any other constituting chemical element in the outermost atomic layer (for example Rh−Ti alloy formation) can be totally excluded on the basis of our LEIS measurements. If we accept the structural model supported by DFT calculation in ref 23, the Ti:O ratio varies in the range of 1.1 and 1.3 due to the slightly different oxygen arrangements presented above. The comparison of the XPS Ti 2p and O 1s peak areas obtained on the clean TiO_2(110) surface with the XPS areas for a complete Rh film encapsulated by the hw-TiO-UTO layer results in the same value of the stoichiometry. The rather small layer thickness (0.07 nm) of

dx.doi.org/10.1021/la4038292 | Langmuir XXXX, XXX, XXX−XXX

this film estimated from the STM measurements is also consistent with the model of $TiO_{\sim 1.2}$ highly relaxed bilayer with a strong bonding to the Rh support. This oxide film has only a mild polar character (negatively charged oxygen outside) as deduced from the work function (WF) measurements presented in our previous work.[44]

To close this chapter, note that not only highly reduced oxide phases form a complete 2D films on different metal surfaces, where they exhibit metal−oxygen bilayer bonded to the support metal surface through the metal cation. It was shown in several cases that the oxygen−metal−oxygen (O-Me-O) trilayers can also form 2D oxide films exhibiting relatively good ordering and wetting, but a weaker bond to the substrate.[16,20,23,52] These latter films showing usually pure moire-pattern are out of the scope of this work; nevertheless, they are very promising 2D nanooxides with self-supporting ability.

4.2. Role of Site-Exchange and Surface Diffusion in Nucleation and Growth of Rh on the hw-TiO-UTO film.

Impingement, diffusion, and nucleation of metal adatoms are the main elementary steps leading to formation of nanostructures in a PVD metal deposition process. Accordingly, in the formation of nanostructures, the atomic ambience at the site of impingement is decisively important, because it determines the further steps of the process. Assuming that the sticking probability is sufficiently large and the metal atom lands on a surface of relatively flat diffusion potential landscape, it will have sufficient energy to diffuse on the surface and to find the site of highest bonding energy. This site is actually the deepest potential minima in the surface diffusion profile in the vicinity of the incidence site. This is a typical situation for a "template" effect, where the periodic deep minima serve as nucleation centers. Moreover, in the case of metal deposits, metal atoms so bonded can even contribute to the deepening of the original potential minimum.[15,24,37] In the case of UTO layers, the so-called periodic "picohole"s are the characteristic sites for this type of effect even at/above room temperature.[24] It was shown by theoretical calculations, however, that the landscape of the diffusion barrier strongly depends also on the chemical nature of the metal adatoms: Pd atoms feel much deeper potential minima in picoholes than Au atoms on the same oxide surface.[36] This behavior provides a special nanotechnological method for growth of $(\text{Metal-1})_1(\text{Metal-2})_n$ bimetallic nanoparticles in a well ordered hexagonal arrangement even for the metals (Metal-2), which alone would not grow in the periodicity of the template.[53,54] Turning back to the Rh/hw-TiO-UTO/Rh system, our STM data suggest that the incoming Rh atoms can leave the UTO films' structure unperturbed and the mean free path of metal adatoms can be so large that part of them can diffuse to the interparticle region of the $TiO_2(110)$ surface (see Figure 8D,E). More frequently, however, the direct interaction between the deposited atom (A_d) and the metal sublayer (M_S) supporting the UTO lattice cannot be neglected. In this way, the bonding between the A_d and M_s dramatically changes the local and periodic diffusion potential map. The probability of this process increases certainly for the UTO layers of high lattice tension. As presented in Figure 10B, the periodic lattice of hw-TiO-UTO exhibits a high level of distortions providing a large probability of capture of both impinging and diffusing Rh atoms to the rhodium sublayer through forming a strong metal−metal bond. It is reasonable to suppose that the energy released by this process weakens the bonding of TiO_{1+x} layer to the support metal and it accelerates the diffusion of a TiO species to the top of the adatoms. This exchange process can be explained also on the basis of surface free energy minimization, because the surface free energy of Rh ($\sim$2.6 J m^{-2})[55] is much higher than that of oxygen-terminated TiO_{1+x} layer ($\sim$1.8 J m^{-2})[22] representing a driving force for the encapsulation of Rh overlayer by the TiO-UTO film. Figure 10C (left side) depicts a simple scheme of the composition of surface−subsurface layers before and during the Rh-post-deposition at different temperatures (230 and 500 K). The growth of Co overlayers on a VO(111) "wagon-wheel" bilayer supported on a Rh(111) surface investigated by STM and XPS exhibited a fairly similar tendency indicating an almost full encapsulation behavior already at room temperature.[16,40] Naturally, by lowering the temperature into the 310−230 K range, more and more metal adatoms are stabilized on top of the UTO layer, as the restructuring of this layer is kinetically hindered. Thermal activation of layer mixing has also been reported for a Pd film deposited on a FeO-UTO film supported on Pt(111), where the annealing in UHV causes the diffusion of Pd underneath the FeO(111) layer.[56,57]

The thermally induced development of the nanostructures formed after the deposition of Rh on the Rh-supported hw-TiO-UTO layer can be characterized as an Ostwald-ripening of 2D nanoparticles (see Figures 6 and 7). In harmony with the commentary above, these 2D nanocrystallites can essentially be identified as Rh nanocrystallites covered by a TiO_{1+x} film on a Rh(111) surface (Figure 10C, right side). Consequently, it seems worth comparing their thermal stability to that of the Rh on Rh(111) system.[58] This latter work reports on a transition temperature ($\sim$600 K) related to a change in the nucleation from fingered to compact particle growth, which can be explained by the activation of the diffusion along of the perimeter (step) edges of the particles at and above this temperature. Moreover, plotting the island density (N) at the low coverage limit as a function of inverse temperature (Arrhenius plot), a break point was detected also at around 600 K, indicating a change in the activation energy.[58] Although the values of N are slightly different (indicating a higher nucleation probability) in our case, the general mechanism of the diffusion seems to be rather similar for both systems. Accordingly, we suggest that the 2D ripening process detected in our case is mainly determined by the Rh on Rh diffusion.

5. SUMMARY

Reproducible formation of ordered hexagonal "wheel" TiO_{1+x} ultrathin (hw-TiO-UTO) decoration films were found on 5−50 ML thick Rh films supported by $TiO_2(110)$ after annealing at high temperatures (max. 1050 K) for a few minutes. As a function of Rh content, two cases were distinguished: (a) in the lower coverage range (5−15 ML), the annealing at 1050 K resulted in stripe-like hw-TiO-UTO-decorated Rh nanoparticles of approximately 30 × 150 nm lateral size, 10−20 atomic layer thickness, and flat top facet of (111); (b) for higher Rh coverages (15−50 ML), the Rh thin layer covered completely also by hw-TiO-UTO film sustained its continuity up to 950 K. The latter case (b) provided a clear XPS evidence of a highly reduced Ti^{2+} state and the comparison of XPS Ti-2p and O-1s intensities suggested an O:Ti = 1.2 stoichiometry. The STM results also disclosed some new fine details of the atomic structure of the hw-TiO-UTO film. Although the overall periodicity and the symmetry detected formerly was confirmed in the present work (hexagonal superlattice with 1.50 ($\pm$0.05) nm unit cell vector), two different arrangements of the bright

dx.doi.org/10.1021/la4038292 | Langmuir XXXX, XXX, XXX−XXX

points forming characteristic triangles were identified. In harmony with previous theoretical simulations, the appearance of bright and dark points (chemical contrast) of the same sublattice of overlayer Ti ions in a hexagonal arrangement with 0.31 (±0.01) nm lattice parameter is attributed to an inhomogeneous oxygen content: the bright points are fourfold and the dark points are threefold oxygen coordinated Ti ions, respectively. The thickness of the hw-TiO-UTO layer was experimentally determined by line profile analysis executed in the region, where tunneling induced local removal of the oxide ultrathin layer was performed previously. On this basis, we have obtained a value of 0.07 (±0.02) nm for the film thickness.

The postdeposition of Rh in different amounts at RT revealed that the ordered hw-TiO-UTO layer becomes strongly disturbed and the adlayer exhibits a 0.2 nm average height. It was found that 2D nanoparticles of 1−2 nm diameter are formed at RT and their average lateral size increases gradually in the temperature range of 300−900 K, probably due to a thermally activated 2D Ostwald-ripening process. Nucleation theory analysis of rhodium particle growth verified that the sintering of postdeposited Rh proceeds directly on the surface of Rh multilayer accompanied by a continuous rebuild of the covering TiO_{1+x} ultrathin film. The careful evaluation of the LEIS intensity data and the CO titration of Rh sites of the particles formed at low temperatures have shown that an exchange of the deposited Rh atoms with the hw-TiO-UTO layer proceeds significantly to an extent of 50% even at around 230 K and this value increases up to 85−90% in the temperature range of 300−500 K. The total disappearance of the characteristic LEIS signal for Rh takes place at ∼900 K, where a complete hw-TiO-UTO covering layer forms (100% exchange) even on top of the postdeposited Rh.

■ AUTHOR INFORMATION

Corresponding Author

*Phone: +36 62 544 646/Fax: +36 62 544 106. aberko@chem.u-szeged.hu.

Notes

The authors declare no competing financial interest.

■ ACKNOWLEDGMENTS

This work was supported by the Hungarian Scientific Research Fund (OTKA) through the K81660 project. The authors gratefully thank the support by the financial sources of TÁMOP-4.2.2/A-11/1/KONV-2012-0047 and COST Actions of CM1104 & CM1301.

■ REFERENCES

(1) Bae, S.; Kim, H.; Lee, Y.; Xu, X.; Park, J.-S.; Zheng, Y.; Balakrishnan, J.; Lei, T.; Kim, H. R.; Song, Y. I.; Kim, Y.-J.; Kim, K. S.; Özyilmaz, B.; Ahn, J.-H.; Hong, B. H.; Iijima, S. Roll-to-roll Production of 30-in. Graphene Films for Transparent Electrodes. *Nat. Nanotechnol.* **2010**, *5*, 574−578.

(2) Wintterlin, J.; Bocquet, M.-L. Graphene on Metal Surfaces. *Surf. Sci.* **2009**, *603*, 1841−1852.

(3) Wang, Q. H.; Kalantar-Zadeh, K.; Kis, A.; Coleman, J. N.; Strano, M. S. Electronics and Optoelectronics of Two-dimensional Transition Metal Dichalcogenides. *Nat. Nanotechnol.* **2012**, *7*, 699−712.

(4) Colson, J. W.; Dichtel, W. R. Rationally Synthesized Two-dimensional Polymers. *Nat. Chem.* **2013**, *5* (6), 453−465.

(5) Yang, J. J.; Strukov, D. B.; Stewart, D. R. Memristive Devices for Computing. *Nat. Nanotechnol.* **2013**, *8*, 13−24.

(6) Pacchioni, G. Two-Dimensional Oxides: Multifunctional Materials for Advanced Technologies. *Chem.—Eur. J.* **2012**, *18*, 10144−10158.

(7) Bowker, M.; Stone, P.; Morrall, P.; Smith, R.; Bennett, R.; Perkins, N.; Kvon, R.; Pang, C.; Fourre, E.; Hall, M. Model Catalyst Studies of the Strong Metal−Support Interaction: Surface Structure Identified by STM on Pd Nanoparticles on TiO2(110). *J. Catal.* **2005**, *234*, 172−181.

(8) Dulub, O.; Hebenstreit, W.; Diebold, U. Imaging Cluster Surfaces with Atomic Resolution: The Strong Metal-Support Interaction State of Pt Supported on TiO_2(110). *Phys. Rev. Lett.* **2000**, *84*, 3646−3649.

(9) Berkó, A.; Ulrych, I.; Prince, K. C. Encapsulation of Rh Nanoparticles Supported on TiO2(110)-(1 × 1) Surface: XPS and STM Studies. *J. Phys. Chem. B* **1998**, *102*, 3379−3386.

(10) Majzik, Z.; Balázs, N.; Berkó, A. Ordered SMSI Decoration Layer on Rh Nanoparticles Grown on TiO_2(110) Surface. *J. Phys. Chem. C* **2011**, *115*, 9535−9544.

(11) Shaikhutdinov, S.; Freund, H.−J. Ultrathin Oxide Films on Metal Supports: Structure-Reactivity Relations. *Annu. Rev. Phys. Chem.* **2012**, *63*, 619−633.

(12) Pang, C. L.; Lindsay, R.; Thornton, G. Structure of Clean and Adsorbate-Covered Single-Crystal Rutile TiO_2 Surfaces. *Chem. Rev.* **2013**, *113*, 3887−3948.

(13) Óvári, L.; Kiss, J. Growth of Rh Nanoclusters on TiO_2(110): XPS and LEIS Studies. *Appl. Surf. Sci.* **2006**, *252*, 8624−8629.

(14) Nilius, N. Properties of Oxide Thin Films and their Adsorption Behavior Studied by Scanning Tunneling Microscopy and Conductance Spectroscopy. *Surf. Sci. Rep.* **2009**, *64*, 595−659.

(15) Freund, H.-J.; Pacchioni, G. Oxide Ultra-thin Films on Metals: New Materials for the Design of Supported Metal Catalysts. *Chem. Soc. Rev.* **2008**, *37*, 2224−2242.

(16) Surnev, S.; Fortunelli, A.; Netzer, F. P. Structure-Property Relationship and Chemical Aspects of Oxide-Metal Hybrid Nanostructures. *Chem. Rev.* **2013**, *113*, 4314−4372.

(17) Tauster, S. J.; Fung, S. C. Strong Metal-Support Interactions: Occurrence among the Binary Oxides of Groups IIA-VB. *J. Catal.* **1978**, *55*, 29.

(18) Bernal, S.; Botana, F. J.; Calvino, J. J.; López, C.; Pérez-Omil, J. A.; Rodrígez-Izquierdo, J. M. High-resolution Electron Microscopy Investigation of Metal-Support Interaction in Rh/TiO_2. *J. Chem. Soc. Faraday Trans.* **1996**, *92* (15), 2799−2809.

(19) Fu, Q.; Wagner, T. Interaction of Nanostructured Metal Overlayers with Oxide Surfaces. *Surf. Sci. Rep.* **2007**, *62*, 431−498.

(20) Männig, A.; Zhao, Z.; Rosenthal, D.; Christmann, K.; Hoster, H.; Rauscher, H.; Behm, R. J. Structure and Growth of Ultrathin Titanium Oxide Films on Ru(0001). *Surf. Sci.* **2005**, *576*, 29−44.

(21) Schoiswohl, J.; Sock, M.; Eck, S.; Surnev, S.; Ramsey, M. G.; Netzer, F. P.; Kresse, G. Atomic-level Growth Study of Vanadium Oxide Nanostructures on Rh(111). *Phys. Rev. B* **2004**, *69*, 155403−13.

(22) Diebold, U. The Surface Science of Titanium Dioxide. *Surf. Sci. Rep.* **2003**, *48*, 53−229.

(23) Barcaro, G.; Cavaliere, E.; Artiglia, L.; Sementa, L.; Gavioli, L.; Granozzi, G.; Fortunelli, A. Building Principles and Structural Motifs in TiO_x Ultrathin Films on a (111) Substrate. *J. Chem. Phys.* **2012**, *116*, 13302−13306.

(24) Gavioli, L.; Cavaliere, E.; Agnoli, S.; Barcaro, G.; Fortunelli, A.; Granozzi, G. Template-assisted Assembly of Transition Metal Nanoparticles on Oxide Ultrathin Films. *Prog. Surf. Sci.* **2011**, *86*, 59−81.

(25) Sedona, F.; Rizzi, G. A.; Agnoli, S.; Llabrés i Xamena, F. X.; Papageorgiou, A.; Ostermann, D.; Sambi, M.; Finetti, P.; Schierbaum, K.; Granozzi, G. Ultrathin TiO_x Films on Pt(111): A LEED, XPS, and STM Investigation. *J. Phys. Chem. B* **2005**, *109*, 24411−24426.

(26) Sedona, F.; Agnoli, S.; Granozzi, G. Ultrathin Wagon-Wheel-like TiOx Phases on Pt(111): A Combined Low-Energy Electron Diffraction and Scanning Tunneling Microscopy Investigation. *J. Phys. Chem. B* **2006**, *110* (31), 15359−15367.

(27) Szökő, J.; Berkó, A. Tunnelling Spectroscopy of Pt Nanoparticles Supported on TiO_2(110) Surface. *Vacuum* **2003**, *71*, 193−199.
(28) Herman, G. S.; Gallagher, M. C.; Joyce, S. A.; Peden, C. H. F. Structure of Epitaxial Thin TiO_x Films on W(110) as Studied by Low Energy Electron Diffraction and Scanning Tunneling Microscopy. *J. Vac. Sci. Technol. B* **1996**, *14* (2), 1126−1130.
(29) Berkó, A.; Balázs, N.; Kassab, G.; Óvári, L. Segregation of K and its Effects on the Growth, Decoration, and Adsorption Properties of Rh Nanoparticles on TiO2(110). *J. Catal.* **2012**, *289*, 179−189.
(30) Bennett, R. A.; Pang, C. P.; Perkins, N.; Smith, R. D.; Morrall, P.; Kvon, R. I.; Bowker, M. Surface Structures in the SMSI State; Pd on (1 × 2) Reconstructed TiO_2(110). *J. Phys. Chem. B* **2002**, *106*, 4688.
(31) Bennett, R. A.; McCavish, R. D. Non-Stoichiometric Oxide Surfaces and Ultra-thin Films: Characterisation of TiO_2. *Top. Catal.* **2005**, *36*, 11.
(32) Sedona, F.; Granozzi, G.; Barcaro, G.; Fortunelli, A. Defect Evolution in Oxide Nanophases: The Case of a Zigzag-like TiO_x Phase on Pt(111). *Phys. Rev. B* **2008**, *77*, 115417−115424.
(33) Wang, H. C.; Ogletree, D. F.; Salmeron, M. Scanning Tunneling Microscopy Study of TiO_x on Rh(111). *J. Vac. Sci. Technol. B* **1991**, *9* (2), 853−856.
(34) Surnev, S.; Vitali, L.; Ramsey, M. G.; Netzer, F. P.; Kresse, G.; Hafner, J. Growth and Structure of Ultrathin Vanadium oxide Layers on Pd(111). *J. Phys. Rev. B* **2000**, *61*, 13945−13954.
(35) Schoiswohl, J.; Surnev, S.; Sock, M.; Eck, S.; Ramsey, M. G.; Netzer, F. P.; Kresse, G. Reduction of Vanadium-oxide Monolayer Structures. *Phys. Rev. B* **2005**, *71*, 165437−165444.
(36) Barcaro, G.; Fortunelli, A.; Granozzi, G. Metal Adsorption on Oxide Polar Ultrathin Films. *Phys. Chem. Chem. Phys.* **2008**, *10*, 1876−1882.
(37) Barcaro, G.; Fortunelli, A. Adsorption and Diffusion of Fe on a Titania Ultrathin Film. *J. Phys. Chem. C* **2009**, *113*, 14860−14866.
(38) Pacchioni, G.; Freund, H.-J. Electron Transfer at Oxide Surfaces. The MgO Paradigm: from Defects to Ultrathin Films. *Chem. Rev.* **2013**, *113*, 4035−4072.
(39) Sedona, F.; Sambi, M.; Artiglia, L.; Rizzi, G. A.; Vittadini, A.; Fortunelli, A.; Granozzi, G. Mobility of Au on TiO_x Substrates with Different Stoichiometry and Defectivity. *J. Phys. Chem. C* **2008**, *112*, 3187−3190.
(40) Parteder, G.; Allegretti, F.; Surnev, S.; Netzer, F. P. Growth of Cobalt on a VO(111) Surface: Template, Surfactant or Encapsulant Role of the Oxide Nanolayer? *Surf. Sci.* **2008**, *602*, 2666−2674.
(41) Chen, M. S.; Luo, K.; Kumar, D.; Wallace, W. T.; Yi, C.-W.; Gath, K. K.; Goodman, D. W. The Structure of Ordered Au Films on TiO_x. *Surf. Sci.* **2007**, *601*, 632−637.
(42) Netzer, F. P.; Allegretti, F.; Surnev, S. Low-dimensional Oxide Nanostructures on Metals: Hybrid Systems with Novel Properties. *J. Vac. Sci. Technol.* **2010**, *28*, 1−4.
(43) Berkó, A.; Szökő, J.; Solymosi, F. High Temperature Postgrowing of Pt-nanocrystallites Supported and Encapsulated on TiO_2(110) surface. *Surf. Sci.* **2003**, *532*−*535*, 390−395.
(44) Bugyi, L.; Óvári, L.; Kónya, Z. The Formation and Stability of Rh Nanostructures on TiO_2(1 1 0) Surface and TiO_x Encapsulation layers. *Appl. Surf. Sci.* **2013**, *280*, 60−66.
(45) Óvári, L.; Berkó, A.; Balázs, N.; Majzik, Z.; Kiss, J. Formation of Rh-Au Core-shell Nanoparticles on TiO_2(110) Surface Studied by STM and LEIS. *Langmuir* **2010**, *26* (3), 2167−2175.
(46) Beszeda, I.; Gontier-Moya, E. G.; Beke, D. L. Investigation of Mass Transfer Surface Self-diffusion on Palladium. *Surf. Sci.* **2003**, *547*, 229−238.
(47) Pétigny, S.; Mostéfa-Sba, H.; Domenichini, B.; Lesniewska, E.; Steinbrunn, A.; Bourgeois, S. Superficial Defects Induced by Argon and Oxygen Bombardments on (110) TiO_2 Surfaces. *Surf. Sci.* **1998**, *410*, 250−257.
(48) Sadeghi, H. R.; Heinrich, V. E. Rh on TiO_2: Model Catalyst Studies of the Strong Metal-Support Interaction. *Appl. Surf. Sci.* **1984**, *19*, 330−340.
(49) Bugyi, L.; Óvári, L.; Kiss, J. Formation and Characterization of Rh−Mo Bimetallic Layers on the TiO_2(110) Surface. *Surf. Sci.* **2009**, *603*, 2958−2963.
(50) Weiss, W.; Ranke, W. Surface Chemistry and Catalysis on Well-defined Epitaxial Iron-oxide Layers. *Prog. Surf. Sci.* **2002**, *70*, 1−151.
(51) Zhang, L. P.; vanEk, J.; Diebold, U. Spatial Self-Organization of a Nanoscale Structure on the Pt(111) Surface. *Phys. Rev. B* **1999**, *59* (8), 5837−5846.
(52) Zhang, Y.; Giordano, L.; Pacchioni, G.; Vittadini, A.; Sedona, F.; Finetti, P.; Granozzi, G. The Structure of a Stoichiometric TiO_2 Nanophase on Pt(111). *Surf. Sci.* **2007**, *601*, 3488−3496.
(53) Schmid, M.; Kresse, G.; Buchsbaum, A.; Napetschnig, E.; Gritschneder, S.; Reichling, M.; Varga, P. Nanotemplate with Holes: Ultrathin Alumina on Ni_3Al(111). *Phys. Rev. Lett.* **2007**, *99*, 196104−196107.
(54) Buchsbaum, A.; DeSantis, M.; Tolentino, H. C. N.; Schmid, M.; Varga, P. Highly Ordered Pd, Fe, and Co Clusters on Alumina on Ni_3Al(111). *Phys. Rev. B* **2010**, *81*, 115420−115431.
(55) Vitos, L.; Ruban, A. V.; Skriver, H. L.; Kollár, J. The Surface Energy of Metals. *Surf. Sci.* **1998**, *411*, 186−202.
(56) Meyer, R.; Lahav, D.; Schalow, T.; Laurin, M.; Brandt, B.; Schauermann, S.; Guimond, S.; Klüner, T.; Kuhlenbeck, H.; Libuda, J.; Shaikhutdinov, S.; Freund, H.-J. CO Adsorption and Thermal Stability of Pd Deposited on a Thin FeO(111) Film. *Surf. Sci.* **2005**, *586*, 174−182.
(57) Dohnálek, Z.; Kim, J.; Kay, B. D. Growth of Epitaxial Thin Pd(111) Films on Pt(111) and Oxygen-terminated FeO(111) Surfaces. *Surf. Sci.* **2006**, *600*, 3461−3471.
(58) Tsui, F.; Wellman, J.; Uher, C.; Clarke, R. Morphology Transition and Layer-by-Layer Growth of Rh(111). *Phys. Rev. Lett.* **1996**, *76* (17), 3164−3167.